This article has been accepted for publication in a future issue of this journal, but has not been fully edited. Content may change prior to final publication. Citation information: DOI 10.1109/JESTPE.2021.3099476, IEEE Journal of Emerging and Selected Topics in Power Electronics

A Bidirectional Symmetrical C4LC-DCX Resonant Converter with Power Limitation Capability

Guo Xu, *Member, IEEE*, Junyi Huang, *Student Member, IEEE*, Hanbing Dan, *Member, IEEE*, Mei Su, *Member, IEEE* and Runmin Zou, *Member, IEEE*

***Abstract*—To achieve the maximum efficiency of resonant converter under wide voltage conversion gain range, two stage conversion, which adopts the resonant converter operating at resonant frequency to work as a dc-dc transformer (DCX) in isolation stage, is a preferred solution. This paper proposes a bidirectional C4LC resonant converter to work as a DCX. The structure of the topology is totally symmetrical, and two auxiliary inductors are used to achieve full load range zero-voltage-switching (ZVS) for all the power switches under bidirectional power flow. Unlike conventional ZVS analysis, the ZVS of the proposed converter is analyzed with considerations of all the switch junction capacitors and load. The clamping diodes are also combined in the topology which can help achieve natural power limitation in case of overload and limit the start-up current. Even though four inductors and one transformer are illustrated in the topology, all these magnetic components can be simplified and manufactured with one external inductor and one conventional transformer. Meanwhile, the converter operates at fixed frequency and adopts the synchronous Pulse Width Modulation (PWM) modulation, which can achieve constant voltage gain and automatically change the power direction without synchronous rectifier (SR) current detection. Finally, the experimental results from a 1-kW prototype verify the effectiveness of the proposed converter.**

***Index Terms*—natural bidirectional power flow, power limitation, symmetrical C4LC-DCX resonant converter, ZVS.**

I. Introduction

ISOLATED DC/DC converter can provide an interface between power bus and energy storage device [1], and it is widely used in distributed power system, uninterruptible power supply (UPS) and electrical vehicles to realize power conversion and satisfy the safety requirement [2].

Among the various topologies of isolated DC/DC converters [3]-[7], resonant converters, such as LLC converter, CLLC converter, etc., have been a preferred solution, due to their high performance in view of soft switching and electromagnetic interference (EMI) performance [8].

For LLC resonant converter, within a specific frequency range, it can achieve ZVS turn-on of the primary side switches and zero-current-switching (ZCS) turn-off of the secondary side switches [9]. When operating at the resonant frequency, the conversion efficiency of LLC resonant converter reaches the highest. However, if the working frequency is away from the resonant point when wide conversion gain range is required, the conversion efficiency will decrease because of the increasing circulating current [10].

To cope with the contradiction between wide range of voltage gain regulation and high conversion efficiency, two stage conversion structure is studied in [11]-[13]. As shown in Fig. 1, the first stage is a LLC resonant converter which operates at the resonant point to achieve its best efficiency. The conversion gain of the LLC-DCX is unregulated. The second stage usually is a none-isolated DC/DC converter (e.g., buck converter, boost converter and buck-boost converter) with PWM modulation, which is used as a voltage regulator to adjust the voltage gain [14]-[16]. The feedback loop of the second-stage converter doesn't need to be isolated, therefore the dynamic response of the voltage regulation module is improved. The LLC-DCX in the first stage adopts open-loop control, so it is simple to implement.

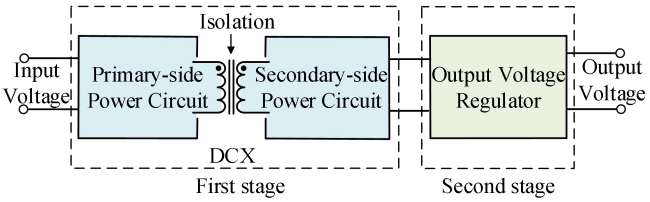

Fig. 1. The structure of the two-stage conversion.

In order to improve the efficiency of LLC-DCX, many methods have been proposed. In [17] and [18], resonant frequency tracking methods are applied to make the LLC resonant converter exactly work at the resonant point to obtain the best efficiency. In [19], a method of multilevel gate driver is proposed, which can boost the efficiency of LLC-DCX by reducing the effect of parasitic inductance to solve the early SR-switch turn-off problem. However, in the above methods, current sensing or voltage sensing is required for the SR switches, which increases the cost and makes the control strategy more complex. Additionally, in [20], the primary side of LLC converter is dynamically changed from full bridge structure to half bridge structure under light load condition, which significantly improves the overall light load efficiency. In [21], a matrix transformer structure and PCB windings are

Manuscript received February 8, 2020; revised April 16, 2021; accepted July 17, 2021. This work was supported in part by the National Nature Science Foundation of China under Grant 61903382, the StateKey Laboratory of Power System and Generation Equipment under Grant SKLD21KM06, the Natural Science Foundation of Hunan Province, China under Grant 2020JJ5722, the National Science Fund for Young Scholars of China under Grant 51907206. (Corresponding author: Hanbing Dan.)

G. Xu, J. Huang, H. Dan, M. Su and R. Zou are with the School of Automation, Central South University and with Hunan Provincial Key Laboratory of Power Electronics Equipment and Grid, Changsha, 410083, China, (e-mail: xuguocsu@csu.edu.cn; Huangjunyi@csu.edu.cn; daniel698@sina.cn; sumeicsu@csu.edu.cn; rmzou@csu.edu.cn).

This article has been accepted for publication in a future issue of this journal, but has not been fully edited. Content may change prior to final publication. Citation information: DOI 10.1109/JESTPE.2021.3099476, IEEE Journal of Emerging and Selected Topics in Power Electronics

applied in LLC-DCX to reduce the losses of transformer. Although these methods can achieve high efficiency for LLC-DCX, they are not suitable for bidirectional power applications.

For bidirectional power applications, symmetrical structure is required to ensure that the operational characteristics of the converter will not change with the power direction. A symmetrical bidirectional CLLLC resonant converter is proposed in [22]-[23], which has the same operation characteristics in the forward and backward power directions. In [24], a bidirectional L3C resonant converter is proposed, which has a symmetrical resonant tank in bidirectional power flow. In [25], four diodes are added in the half-bridge LLC converter to help achieve the same operation characteristics in the forward and backward modes. However, even if these methods [22]-[25] are applied in LLC-DCX, the control logics need to be changed according to the direction of power flow, it's difficult to shift the power direction smoothly.

In [26] and [27], synchronous PWM modulation method is applied in LLC-DCX to achieve natural bidirectional power flow. The driving signals for the primary and secondary side switches are identical, which avoids SR sensing and logics exchanging for two sides switches when the power direction changes. However, only one side switches of the LLC converter in [26] and [27] can achieve ZVS. In order to boost the efficiency, a bidirectional LLC resonant converter with an auxiliary inductor is proposed in [28]. In this converter, all the switches can achieve ZVS under bidirectional power flow. However, one transformer and two external inductors are used in the hardware circuit, which reduces the power density of the circuit. In view of ZVS analysis, the effect of load and junction capacitors of secondary side switches is ignored in [26] and [27], and ZVS is analyzed without consideration of switches junction capacitors in [28]. As pointed out in [29], the secondary side junction capacitors can cause the inconsistent charge/discharge time, hence the ZVS analysis in [26]-[28] leads to insufficient accuracy. Even though the resonant converter is working as DCX, the operation modes for the converter in [26]-[28] are not identical under different power directions, which would further increase the complexity of full load range ZVS analysis and achievement when considering the junction capacitors and load.

In addition, over current protection and power limitation capability are not embedded in these methods [26]-[28]. When the converter is over load or starting up, the current and voltage stress on the resonant tank is extreme high which may damage the circuit. To deal with these issues, in [30], a Pulse Frequency Modulation (PFM)/PWM hybrid control method is applied in LLC resonant converter, which can achieve current limitation effectively. However, this method requires additional circuits to detect the over load conditions. Reference [31] proposes a multi-element resonant tank which combines notch filter and band pass filter. In case of over current, the switching frequency is increased to notch frequency to limit the output current. By this method, the current can be limited inherently by the characteristic of resonant tank, but sensing devices are required. In [32], an auxiliary circuit is added in the LLC converter, which can clamp the voltage of resonant capacitor by the output voltage through a transformer under over current condition. By this method, inherent current limitation ability is embedded, but the extra transformer increases the cost and volume of the converter. In [33], clamping diodes are added to bypass the resonant capacitors in case of over current, which can effectively reduce the input current ripple, switch current and resonant capacitor voltage stress. This method is simple to implement and its response is fast. However, the clamping diodes are only added at one side of the converter, which is only suited for unidirectional power transfer.

The proposed C4LC-DCX resonant converter has the following advantages:

1) The proposed converter with the synchronous PWM modulation method has identical operation characteristics under bidirectional power directions and can achieve natural bidirectional power flow. In addition, the resonant inductor currents in the primary and secondary sides are symmetrical, which simplifies the analysis of voltage conversion gain and ZVS.
2) Full-load range ZVS can be achieved for all the switches under bidirectional power flow due to the two auxiliary inductors added in the proposed converter. The ZVS is analyzed with considerations of all the switch junction capacitors and load, which provides more accurate guidance for ZVS design. Moreover, a method of magnetic components integration is proposed, by which all the magnetic components can be simplified and manufactured with one external inductor and one conventional transformer, and the specific design considerations are comprehensively discussed.
3) Power limitation and over current protection can be achieved under bidirectional power flow since the clamping diodes are connected in parallel with the resonant capacitors at both sides of the proposed converter.

In this paper, a bidirectional symmetrical C4LC-DCX resonant converter with power limitation capability is proposed to achieve natural bidirectional power flow and ZVS with consideration of load and all the switches junction capacitors. The operation principle analysis of the C4LC-DCX resonant converter with the synchronous PWM modulation method is given in Section II. In Section III, the constant voltage gain, ZVS condition, power limitation and magnetic components integration of the C4LC-DCX converter are analyzed. The experimental results based on a 1-kW prototype are shown in Section IV to verify the effectiveness of the proposed converter.

II. Principle of Operation

A. Topology Structure

The topology of the C4LC-DCX resonant converter is shown in Fig. 2. In this converter, two active half bridges are applied to achieve bidirectional power flow. In the primary side of the transformer, the auxiliary inductor L_{a1} is connected between point A and point B, and in the secondary side, the auxiliary inductor L_{a2} is connected between point C and point D. The two auxiliary inductors are used to help achieve full-load range ZVS for the switches of the proposed converter, and they affect the resonant frequency and the resonant

This article has been accepted for publication in a future issue of this journal, but has not been fully edited. Content may change prior to final publication. Citation information: DOI 10.1109/JESTPE.2021.3099476, IEEE Journal of Emerging and Selected Topics in Power Electronics

process. Clamping diodes are in parallel with the resonant capacitors to realize power limitation in case of overload and limit the inrush current when the converter starts up. It should be noted that even though four inductors and one transformer are illustrated in the topology, all these magnetic components can be simplified and manufactured with one external inductor and one conventional transformer, which will be explained in Part D of Section III.

The turns ratio of the transformer is n. To ensure that the topology is completely symmetrical, the value of L_{r2} referred to the primary side is equal to L_{r1} ($L_{r1}=n^2L_{r2}=L_r$), the value of C_{r3} and C_{r4} referred to the primary side is equal to C_{r1} and C_{r2} ($C_{r1}=C_{r2}=C_{r3}/n^2=C_{r4}/n^2=C_r$), and the value of L_{a2} referred to the primary side is equal to L_{a1} ($L_{a1}=n^2L_{a2}=L_a$).

With the synchronous PWM modulation method, the driving signals of S_3 and S_4 are the same as those of S_1 and S_2, respectively. If ignoring the effect of the dead-band, the switches S_1 and S_2 in the primary side are switched complementarily with 50% duty cycle (detailed waveforms are shown in Fig. 4). The C4LC-DCX resonant converter operates at the resonant point. Four resonant capacitors C_{r1}, C_{r2}, C_{r3}, C_{r4}, two auxiliary inductors L_{a1}, L_{a2} and two resonant inductors L_{r1}, L_{r2} build up the resonant tank.

In this paper, the forward mode refers to the transmission of power from the V_1 side to the V_2 side.

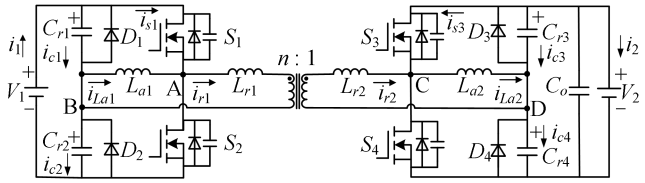

Fig. 2. The topology of the C4LC-DCX resonant converter.

B. Mode 1: Forward Power Transmission Mode

As shown in Fig. 3, in the forward power transmission mode, there are three working stages in a half switching cycle. Fig. 4 shows the key waveforms of the converter in this mode. The proposed converter with synchronous PWM modulation method will not work in DCM (Discontinuous Conduction Mode) mode since the driving signals for two sides switches are identical.

Stage 1 (t_0-t_1): Fig. 3(a) shows the equivalent circuit of the converter in this stage, and it can be equivalently represented by the circuit shown in Fig. 5. At t_0, the switches S_1 and S_3 turn on with ZVS.

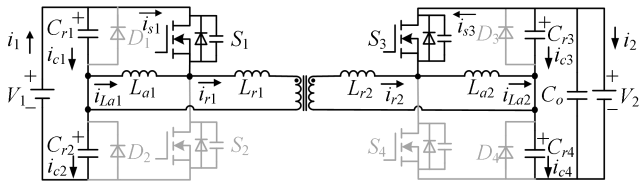

(a)

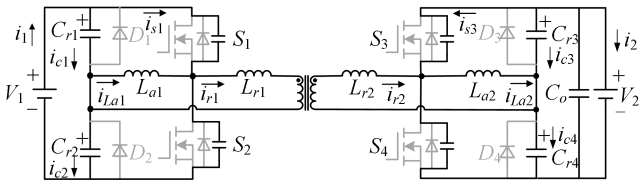

(b)

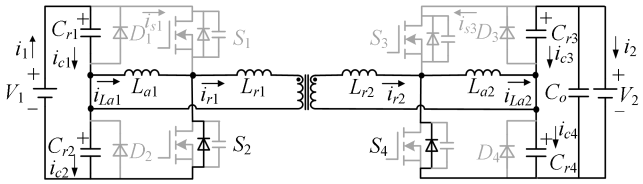

(c)

Fig. 3. The working stages of the converter in the forward power transmission mode.
(a)Stage 1(t_0-t_1). (b)Stage 2(t_1-t_2). (c)Stage 3(t_2-t_3).

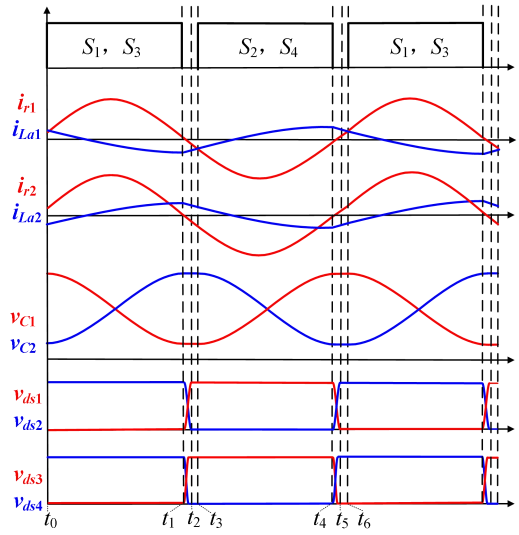

Fig. 4. The key waveforms of the converter in the forward power transmission mode.

In this stage, L_{a1}, L_{a2} resonant with C_{r1}, C_{r2}, C_{r3}, C_{r4}, L_{r1} and L_{r2}. According to the relationship between the voltages and currents of the circuit shown in Fig. 5, the equations (1), (2) and (3) can be deduced to describe the converter in this stage.

$$\begin{cases} 2L_r\dfrac{di_{r1}(t)}{dt}=v_{C1}(t)-nv_{C3}(t) \\ L_a\dfrac{di_{La1}(t)}{dt}=-v_{C1}(t) \\ \dfrac{L_a}{n}\dfrac{di_{La2}(t)}{dt}=nv_{C3}(t) \end{cases} \tag{1}$$

$$\begin{cases} C_r\dfrac{dv_{C1}(t)}{dt}+i_{r1}(t)=C_r\dfrac{dv_{C2}(t)}{dt}+i_{La1}(t) \\ C_rn\dfrac{dv_{C3}(t)}{dt}+\dfrac{i_{La2}(t)}{n}=i_{r1}(t)+C_rn\dfrac{dv_{C4}(t)}{dt} \end{cases} \tag{2}$$

$$\begin{cases} v_{C1}(t)+v_{C2}(t)=V_1 \\ v_{C3}(t)+v_{C4}(t)=V_2 \end{cases} \tag{3}$$

Where i_{r1} is the resonant current in the primary side, i_{La1} and i_{La2} are the currents of L_{a1} and L_{a2} respectively, v_{C1}, v_{C2}, v_{C3} and v_{C4} are the voltages across C_{r1}, C_{r2}, C_{r3} and C_{r4} respectively.

For the proposed C4LC-DCX converter, the resonant frequency is referred to the frequency of the resonant inductor current. According to (1), the current of the resonant inductor in the primary side can be expressed as

$$i_{r1}(t)=\frac{1}{2L_r}\int\left[v_{C1}(t)-nv_{C3}(t)\right]dt \tag{4}$$

Based on (4), it can be deduced that the resonant frequency

This article has been accepted for publication in a future issue of this journal, but has not been fully edited. Content may change prior to final publication. Citation information: DOI 10.1109/JESTPE.2021.3099476, IEEE Journal of Emerging and Selected Topics in Power Electronics

is equal to the frequency of v_{C1}-nv_{C3}. Hence, the resonant frequency can be solved according to the frequency of v_{C1}-nv_{C3}.

According to (3), it can be deduced that $dv_{C2}(t)/dt$=-$dv_{C1}(t)/dt$ and $dv_{C4}(t)/dt$=-$dv_{C3}(t)/dt$, then (2) can be simplified as

$$\begin{cases} 2C_r \dfrac{dv_{C1}}{dt} = i_{La1}(t) - i_{r1}(t) = -i_{s1}(t) \\ 2C_r n \dfrac{dv_{C3}}{dt} = i_{r1}(t) - \dfrac{i_{La2}(t)}{n} = -\dfrac{i_{s3}(t)}{n} \end{cases} \tag{5}$$

The derivative of the difference between the two equations in (5) can be expressed as

$$2C_r \frac{d^2\left[v_{C1}(t) - nv_{C3}(t)\right]}{dt^2} = \frac{di_{La1}(t)}{dt} + \frac{1}{n}\frac{di_{La2}(t)}{dt} - 2\frac{di_{r1}(t)}{dt} \tag{6}$$

Then, substituting the three equations in (1) into (6), it can be deduced that

$$\frac{d^2(v_{C1} - nv_{C3})}{dt^2} + \frac{L_r + L_a}{2L_r L_a C_r}(v_{C1} - nv_{C3}) = 0 \tag{7}$$

By solving the differential equation in (7), the angular frequency of v_{C1}-nv_{C3} can be obtained.

$$\omega_{C13} = \sqrt{\frac{L_r + L_a}{2L_r L_a C_r}} \tag{8}$$

According to the relationship between the resonant current i_{r1} and v_{C1}-nv_{C3} shown in (4), it can be deduced that the resonant angular frequency is equal to the angular frequency of v_{C1}-nv_{C3}. Therefore, the resonant frequency can be expressed as

$$f_r = \frac{\omega_r}{2\pi} = \frac{\omega_{C13}}{2\pi} = \frac{1}{2\pi}\sqrt{\frac{L_r + L_a}{2L_r L_a C_r}} \tag{9}$$

The following equations can be deduced by substituting (1) into the derivative of the sum of the two equations in (5).

$$\frac{d^2(v_{C1} + nv_{C3})}{dt^2} + \frac{1}{2L_a C_r}(v_{C1} + nv_{C3}) = 0 \tag{10}$$

According to the solutions of the differential equations in (7) and (10), the expressions of v_{C1} and v_{C3} can be obtained. Then according to the relationship between switch currents and resonant capacitor voltages in (5), the expressions of switch currents can be deduced. Finally, substituting the initial values of switch currents and resonant capacitor voltages at t_0, the following equations can be deduced

$$\begin{cases} v_{C1}(t) = \dfrac{\frac{I_{S30}}{n} - I_{S10}}{4\omega_r C_r}\sin\omega_r(t-t_0) + \dfrac{V_{C10} - nV_{C30}}{2}\cos\omega_r(t-t_0) \\ \quad - \dfrac{\frac{I_{S30}}{n} + I_{S10}}{4\omega_2 C_r}\sin\omega_2(t-t_0) + \dfrac{V_{C10} + nV_{C30}}{2}\cos\omega_2(t-t_0) \\ nv_{C3}(t) = -\dfrac{\frac{I_{S30}}{n} - I_{S10}}{4\omega_r C_r}\sin\omega_r(t-t_0) - \dfrac{V_{C10} - nV_{C30}}{2}\cos\omega_r(t-t_0) \\ \quad - \dfrac{\frac{I_{S30}}{n} + I_{S10}}{4\omega_2 C_r}\sin\omega_2(t-t_0) + \dfrac{V_{C10} + nV_{C30}}{2}\cos\omega_2(t-t_0) \end{cases} \tag{11}$$

Where V_{C10} is the voltage of C_{r1} at $t = t_0$, I_{s10} is the current of S_1 at $t = t_0$, V_{C30} is the voltage of C_{r3} at $t = t_0$, I_{s30} is the current of S_3 at $t = t_0$, ω_r=$2\pi f_r$, and $\omega_2 = \sqrt{1/\left(2L_a C_r\right)}$.

The equation (11) is complex, in order to simplify the analysis of ZVS condition, the effect of resonance between the resonant capacitors and auxiliary inductors is ignored. Then the resonant capacitor voltage is a sine wave with an angular frequency of ω_r, according to the solution of the differential equation in (7), the voltages of resonant capacitors can be expressed as

$$\begin{cases} v_{C1}(t) = A_1 \sin\omega_r(t-t_0) + B_1 \cos\omega_r(t-t_0) + C \\ v_{C3}(t) = A_2 \sin\omega_r(t-t_0) + B_2 \cos\omega_r(t-t_0) + \dfrac{C}{n} \end{cases} \tag{12}$$

Where A_1, A_2, B_1, B_2 and C are constant quantities remaining to be solved. The absolute values of i_{C1} and i_{C2} are equal, and the sum of v_{C1} and v_{C2} is equal to V_1, hence the DC component of v_{C1}, which is C in (12), is equal to $V_1/2$. Substituting (12) into (5), the currents of S_1 and S_3 in this stage can be expressed by

$$\begin{cases} i_{s1}(t) = -2C_r\omega_r A_1 \cos\omega_r(t-t_0) + 2C_r\omega_r B_1 \sin\omega_r(t-t_0) \\ i_{s3}(t) = -2n^2 C_r\omega_r A_2 \cos\omega_r(t-t_0) + 2n^2 C_r\omega_r B_2 \sin\omega_r(t-t_0) \end{cases} \tag{13}$$

Then substituting the initial values of switch currents and resonant capacitor voltages at t_0 into (12) and (13), the constant quantities A_1, B_1, A_2 and B_2 can be deduced, which are equal to -$I_{S10}/2C_r\omega_r$, V_{C10}-$V_1/2$, -$I_{S30}/2n^2C_r\omega_r$ and V_{C30}-$V_2/2$ respectively.

Therefore, the currents of S_1 and S_3 and the voltages of C_{r1} and C_{r3} in this stage can be expressed by

$$\begin{cases} i_{s1}(t) = 2C_r\omega_r(V_{C10} - \dfrac{V_1}{2})\sin\omega_r(t-t_0) + I_{s10}\cos\omega_r(t-t_0) \\ v_{C1}(t) = (V_{C10} - \dfrac{V_1}{2})\cos\omega_r(t-t_0) - \dfrac{I_{s10}}{2C_r\omega_r}\sin\omega_r(t-t_0) + \dfrac{V_1}{2} \\ i_{s3}(t) = 2n^2C_r\omega_r(V_{C30} - \dfrac{V_2}{2})\sin\omega_r(t-t_0) + I_{s30}\cos\omega_r(t-t_0) \\ v_{C3}(t) = (V_{C30} - \dfrac{V_2}{2})\cos\omega_r(t-t_0) - \dfrac{I_{s30}}{2n^2C_r\omega_r}\sin\omega_r(t-t_0) + \dfrac{V_2}{2} \end{cases} \tag{14}$$

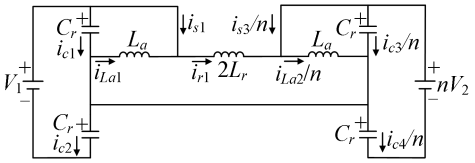

Fig. 5. The equivalent circuit in stage 1 of the forward power transmission.

Stage 2 (t_1-t_2): At t_1, S_1 and S_3 turn off. As shown in Fig. 3(b), in this stage, the junction capacitors of S_1 and S_3 are charged, and the junction capacitors of S_2 and S_4 are discharged. At t_2, the voltages of S_2 and S_4 are equal to zero, the body diodes of S_2 and S_4 conduct.

Stage 3 (t_2-t_3): Fig. 3(c) shows the equivalent circuit of the converter in this stage. In this stage, current flows through the body diodes of S_2 and S_4. At t_3, S_2 and S_4 turn on with ZVS.

Because of the symmetry for both the topology and PWM modulation, the operation principle of the backward power transmission mode is the same as that of the forward power transmission mode.

The initial values of the inductor currents and resonant capacitor voltages at t_0 are solved as follows.

This article has been accepted for publication in a future issue of this journal, but has not been fully edited. Content may change prior to final publication. Citation information: DOI 10.1109/JESTPE.2021.3099476, IEEE Journal of Emerging and Selected Topics in Power Electronics

Considering that the dead-time is relatively short compared with the switching period, the effect of dead-time is ignored in the following analysis. During t_0 to t_1, the input current i_1 is equal to $i_{s1}/2$. Based on power conservation law of two sides, it can be deduced that

$$\overline{i_1} = \frac{2}{T_s}\int_{t_0}^{t_1}\frac{i_{S1}(t)}{2}dt = \frac{V_2^2}{R_o V_1} \tag{15}$$

Where R_o is the output resistance. Hence, substituting the expression of i_{s1} in (14) into (15), V_{C10} can be expressed as

$$V_{C10} = \frac{V_2^2}{4 f_s C_r R_o V_1} + \frac{V_1}{2} \tag{16}$$

In practical application, the output capacitor C_o is designed to be much larger than the resonant capacitor, hence the effect of output capacitor is negligible. The output current i_2 is equal to $-i_{s3}/2$ during t_0 to t_1. The average value of the output current can be expressed as

$$\overline{i_2} = -\frac{2}{T_s}\int_{t_0}^{t_1}\frac{i_{S3}(t)}{2}dt = \frac{V_2}{R_o} \tag{17}$$

Then substituting the expression of i_{s3} in (14) into (17), V_{C30} can be deduced.

$$V_{C30} = \frac{V_2}{2} - \frac{V_2}{4n^2 f_s C_r R_o} \tag{18}$$

As shown in Fig. 5, during t_0 to t_1, the voltage across L_{a1} is equal to $-v_{C1}$, and the voltage across L_{a2} is equal to v_{C3}. Since I_{S10} and I_{S30} are small, their effects on v_{C1} and v_{C3} are ignored in the following analysis. Hence according to (1) and the expressions of v_{C1} and v_{C3} in (14), the following equations can be deuced.

$$i_{La1}(t) = -\frac{2V_{C10} - V_1}{2L_a\omega_r}\sin\omega_r(t-t_0) - \frac{V_1}{2L_a}(t-t_0) + I_{La10} \tag{19}$$

$$i_{La2}(t) = \frac{2V_{C30} - V_2}{2L_a\omega_r}n^2\sin\omega_r(t-t_0) + \frac{n^2V_2}{2L_a}(t-t_0) + I_{La20} \tag{20}$$

Where I_{La10} and I_{La20} are the currents of L_{a1} and L_{a2} at t_0, respectively. I_{La10} is equal to $-i_{La1}(T_r/2)$, and I_{La20} is equal to $-i_{La2}(T_r/2)$. Therefore, according to (19) and (20), it can be deduced that

$$I_{La10} = -i_{La1}(\frac{T_r}{2}) = \frac{V_1 T_r}{8L_a} \tag{21}$$

$$I_{La20} = -i_{La2}(\frac{T_r}{2}) = -\frac{n^2V_2T_r}{8L_a} \tag{22}$$

Where $T_r=1/f_r$. By substituting (16) into the expression of v_{C1} in (14), the voltage across C_{r1} at t_1 can be expressed by (23).

$$v_{C1}(t_1) \approx v_{C1}(\frac{T_r}{2}) = \frac{V_1}{2} - \frac{V_2^2}{4 f_s C_r R_o V_1} \tag{23}$$

The C4LC-DCX converter with synchronous PWM modulation method operates at the resonant frequency, hence the resonant inductor current at t_1 is equal to zero. Since the dead-time is short, the change of v_{C1} during the dead-time is negligible. If ignoring the effect of the switch junction capacitors, during t_1 to t_3, the body diode of S_2 is conducted, and the voltage of the transformer in the primary side v_{T1} is nearly equal to $-V_1/2$. Hence the expression of i_{r1} during t_1 to t_3 can be expressed as

$$i_{r1}(t) = \frac{1}{L_r}\left[v_{C1}(t_1) - \frac{V_1}{2}\right](t-t_1) \tag{24}$$

Then substituting (23) into (24), it can be deduced that

$$I_{r10} = -i_{r1}(t_3) = \frac{P_o t_{dead}}{4 f_s C_r L_r V_1} \tag{25}$$

Where P_o is the output power and t_{dead} is the length of the dead-time. Then according to (21), (22) and (25), the following equation can be deduced.

$$I_{S10} = I_{r10} - I_{La10} = \frac{P_o t_{dead}}{4 f_s C_r L_r V_1} - \frac{V_1 T_r}{8L_a} \tag{26}$$

$$I_{S30} = I_{La20} - nI_{r10} = -\frac{n^2V_2T_r}{8L_a} - \frac{nP_o t_{dead}}{4 f_s C_r L_r V_1} \tag{27}$$

The above equations will be used in the converter characteristics analysis in Section III.

For the conventional LLC converter, the asymmetric structure leads to different operation characteristics in the forward and backward modes and makes the ZVS analysis complex when considering all the switch junction capacitors [34]. The CLLC converter differs from the proposed C4LC-DCX converter in that no auxiliary inductor is added in the converter, hence ZVS cannot be achieved for the switches. For the CLLLC converter [22]-[23], the resonant inductor current is coupled with the magnetizing inductance current, which makes the ZVS analysis with consideration of all the switch junction capacitors complex. In addition, with the traditional magnetizing inductance design method [22], only one side switches can achieve ZVS. Even if these converters work under DCX operation, the above problems still exist. Compared with these converters, the proposed C4LC-DCX converter has a symmetrical structure and the resonant inductor current waveforms in the primary and secondary sides are symmetrical ($i_{r1}=i_{r2}/n$), which simplifies the analysis of operation principle and ZVS condition in bidirectional power directions. Full-load range ZVS can be achieved for all the switches in the proposed converter with considerations of switch junction capacitors and load under bidirectional power flow. In addition, bidirectional power limitation capability is embedded in the proposed converter, while power limitation cannot be achieved in the hardware circuits of the conventional LLC, CLLC and CLLLC converters.

C. Mode 2: Forward Power Limitation Mode

When the converter is overload, the current flowing through the resonant capacitors is large, and then the converter will work in the power limitation mode. As it is shown in Fig. 6, in this mode, there are eight working stages in a half switching cycle. Fig. 7 shows the key waveforms of the converter in this mode.

Stage 1 (t_0-t_1): Fig. 6(a) shows the equivalent circuit of the converter in this stage. At t_0, S_1 turns on with ZVS, while the junction capacitor of S_3 begins to be discharged. This stage ends when the voltage across S_3 decreases to zero at t_1.

Stage 2 (t_1-t_2): As shown in Fig. 6(b), D_2 and D_3 conduct in this stage. The input current i_1 is less than zero, and the output is bypassed by D_3. The resonant tank does not work, and the

This article has been accepted for publication in a future issue of this journal, but has not been fully edited. Content may change prior to final publication. Citation information: DOI 10.1109/JESTPE.2021.3099476, IEEE Journal of Emerging and Selected Topics in Power Electronics

power transmission is interrupted.

Stage 3 (t_2-t_3): Fig. 6(c) shows the equivalent circuit of the converter in this stage. At t_2, i_{La2} is equal to i_{r2}, the current of D_3 is equal to zero. Then, D_3 turns off.

Stage 4 (t_3-t_4): At t_3, i_{La1} is equal to i_{r1}, the current of D_2 decreases to zero. Then, D_2 turns off. This stage is the same as the stage 1 in Mode 1. The equivalent circuit of this stage is shown in Fig. 3(a).

Stage 5 (t_4-t_5): At t_4, v_{C4} drops to zero, and then D_4 conducts. As shown in Fig. 6(d), C_{r3} and C_{r4} are bypassed, and the voltage of L_{a2} is clamped to V_2 in this stage.

Stage 6 (t_5-t_6): Fig. 6(e) shows the equivalent circuit of the converter in this stage. At t_5, S_1 and S_3 turn off, and then the junction capacitors of S_1 and S_2 begin to be charged/discharged. i_{La2} minus i_{r2} is less than zero, so the body diode of S_3 conducts in this stage.

Stage 7 (t_6-t_7): Fig. 6(f) shows the equivalent circuit of this stage. At t_6, the voltage across S_2 drops to zero, and then the body diode of S_2 conducts.

Stage 8 (t_7-t_8): Fig. 6(g) shows the equivalent circuit of this stage. v_{C1} decreases to zero at t_7, and then D_1 conducts. At t_8, S_2 turns on with ZVS, while the junction capacitors of S_3 and S_4 begin to be charged or discharged.

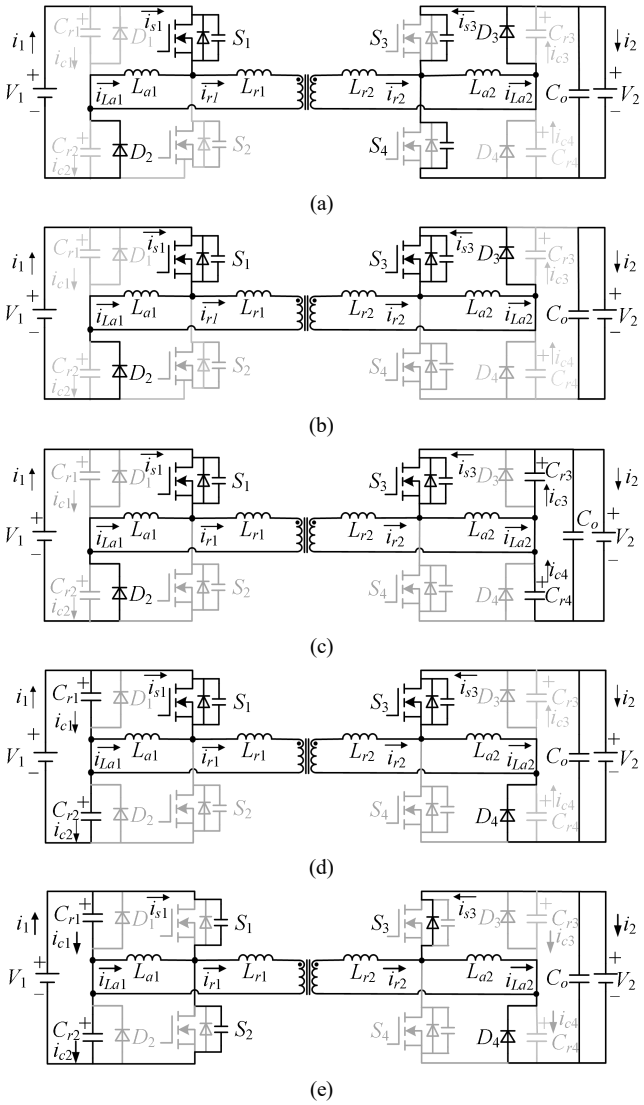

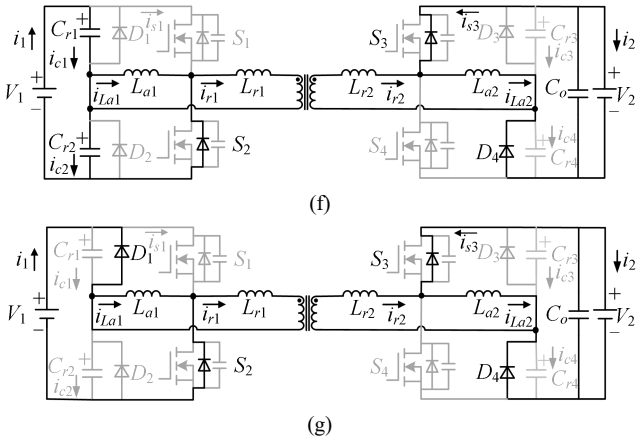

Fig. 6. The working stages of the proposed converter in the forward power limitation mode.
(a)Stage 1(t_0-t_1). (b)Stage 2(t_1-t_2). (c)Stage 3(t_2-t_3). (d)Stage 5(t_4-t_5). (e)Stage 6(t_5-t_6). (f)Stage 7(t_6-t_7). (g)Stage 8(t_7-t_8).

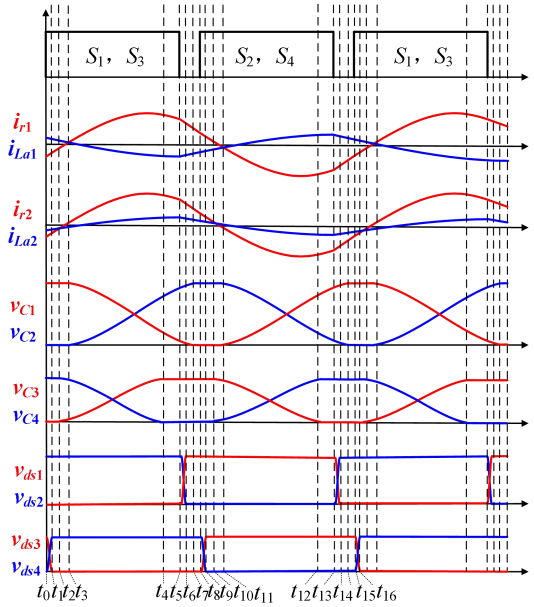

Fig. 7. The key waveforms of the proposed converter in the forward power limitation mode.

It should be noted that the clamping diodes only work in the power limitation mode. Under normal working conditions, it does not participate in the power transmission and will not cause additional loss.

Because of the symmetry for both the topology and PWM modulation, the operation principle of the backward power limitation mode is the same as that of the forward power limitation mode.

III. Converter Characteristics Analysis

A. Constant Voltage Gain

Fig. 8 shows the key currents waveforms of the converter in the forward power transmission mode. Without considering the dead-band, the average value of i_{La1} and i_{La2} is equal to zero. Hence, the average value of the input current i_1 and output current i_2 can be expressed by

$$\overline{i_1} = \frac{2}{T_s}\int_0^{\frac{T_s}{2}} \frac{i_{r1}(t) - i_{La1}(t)}{2}\,dt = \frac{\overline{i_{r1}}}{2} \tag{28}$$

This article has been accepted for publication in a future issue of this journal, but has not been fully edited. Content may change prior to final publication. Citation information: DOI 10.1109/JESTPE.2021.3099476, IEEE Journal of Emerging and Selected Topics in Power Electronics

$$\bar{i}_2 = \frac{2}{T_s}\int_0^{\frac{T_s}{2}} \frac{n i_{r1}(t) - i_{La2}(t)}{2} dt = \frac{n\bar{i}_{r1}}{2} \tag{29}$$

Where T_s is the switching period.

The output power is equal to input power if ignoring the losses, so according to (28) and (29), the voltage conversion gain M can be expressed by

$$M = \frac{V_2}{V_1} = \frac{\bar{i}_1}{\bar{i}_2} = \frac{1}{n} \tag{30}$$

According to (30), a conclusion is drawn that the voltage conversion gain of the proposed converter is only determined by the turns ratio n and its value remains unchanged from no-load to full-load.

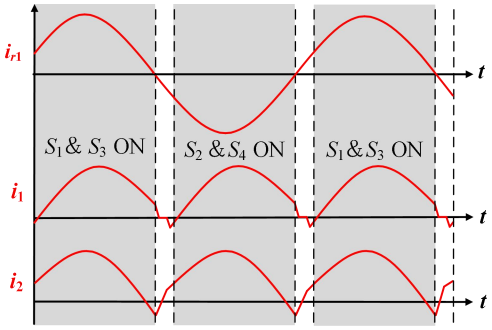

Fig. 8. The key currents waveforms of the converter in the forward power transmission mode.

B. ZVS Condition Analysis

As Fig. 4 shows, to ensure that S_1 and S_2 can achieve ZVS, i_{r1} minus i_{La1} should be positive and can charge/discharge the junction capacitors of S_1 and S_2 completely during t_1 to t_3.

During t_1 to t_3, the voltage of C_{r1} can be regarded as unchanged, and the voltage across S_1 increases from zero to V_1. Hence, it can be deduced that

$$\begin{aligned} i_{La1}(t) &< \frac{1}{L_a}\int_{t_1}^{t}\left[V_1 - v_{C1}(t_1)\right]dt \\ &= \frac{V_1 - v_{C1}(t_1)}{L_a}(t-t_1) + i_{La1}(t_1), \quad \forall t \in [t_1, t_3] \end{aligned} \tag{31}$$

During the dead-time, the voltage of the transformer in the primary side v_{T1} decreases from $V_1/2$ to $-V_1/2$, and v_{T1} plus v_{ds1} is less than or equal to $V_1/2$. Hence, i_{r1} satisfies (32) during t_1 to t_3.

$$\begin{aligned} i_{r1}(t) &> \frac{1}{L_r}\int_{t_1}^{t}\left[v_{C1}(t_1) - \frac{V_1}{2}\right]dt \\ &= \frac{1}{L_r}\left[v_{C1}(t_1) - \frac{V_1}{2}\right](t-t_1), \quad \forall t \in [t_1, t_3] \end{aligned} \tag{32}$$

In order to prevent anti-resonance, i_{r1} minus i_{La1} should be positive during t_1 to t_3. Hence, according to (31) and (32), anti-resonance will not occur if (33) is satisfied.

$$\begin{aligned} i_{r1}(t_3) - i_{La1}(t_3) > \frac{t_{dead}}{L_r}\left[v_{C1}(t_1) - \frac{V_1}{2}\right] - \frac{V_1 - v_{C1}(t_1)}{L_a}t_{dead} \\ - i_{La1}(t_1) > 0 \end{aligned} \tag{33}$$

According to (9), it can be deduced that

$$L_r = \frac{L_a}{8\pi^2 f_r^2 L_a C_r - 1} \tag{34}$$

Then substituting (21), (23) and (34) into (33), it can be deduced that

$$L_a \le \frac{f_s V_1^2 (1 - 4 t_{dead} f_r)}{16\pi^2 t_{dead} P_o f_r^3} \tag{35}$$

In order to discharge or charge the junction capacitors of S_1 and S_2 completely during t_1 to t_3, (36) should be satisfied.

$$\int_{t_1}^{t_3}\left[i_{r1}(t) - i_{La1}(t)\right]dt \ge 2C_{oss1}V_1 \tag{36}$$

Where C_{oss1} is the value of the junction capacitors of the primary side switches. By substituting (21), (23), (31), (32) and (34) into (36), it can be deduced that

$$L_a \le \frac{V_1^2 t_{dead} f_s (1 - 2 f_r t_{dead})}{16 C_{oss1} f_s f_r V_1^2 + 8\pi^2 t_{dead}^2 f_r^3 P_o} \tag{37}$$

From the analysis above, it can be concluded that ZVS for S_1 and S_2 will be achieved if the value of the auxiliary inductors satisfies (35) and (37).

As Fig. 4 shows, in the secondary side, the direction of resonant current i_{r2} during the dead time is favorable for S_3 and S_4 to achieve ZVS. Hence, if (38) is satisfied, the ZVS of the secondary side switches can be achieved.

$$\int_{t_1}^{t_3} i_{La2}(t)dt \ge 2C_{oss2}\frac{V_1}{n} \tag{38}$$

Where C_{oss2} is the value of the junction capacitors of the secondary side switches.

During the dead-time, the change of the secondary side auxiliary inductor current i_{La2} is negligible. Thus, substituting the expression of $i_{La2}(T_r/2)$ in (22) into (38), it can be deduced that

$$L_a \le \frac{n^2 t_{dead}}{16 f_r C_{oss2}} \tag{39}$$

Fig. 9 shows the available region of ZVS according to (35), (37) and (39). To achieved ZVS for all the switches in the proposed C4LC-DCX converter, the auxiliary inductors should be designed to satisfy (35), (37) and (39).

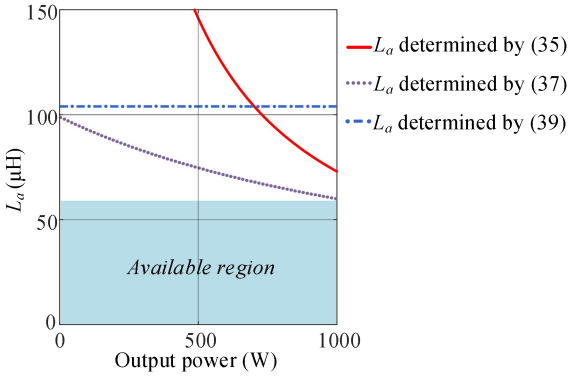

Fig. 9. The available region of ZVS (V_1=400V, n=1, f_r=f_s=500kHz, C_{oss1}=C_{oss2}=60pF, t_{dead}=50ns).

C. Power Limitation of The Converter

In the power limitation mode, the power transmission will be interrupted when the clamping diodes conduct. The maximum transmission power occurs at the critical moment when the load increases to the point where power limitation occurs, and the waveforms at this moment is shown in Fig. 10.

This article has been accepted for publication in a future issue of this journal, but has not been fully edited. Content may change prior to final publication. Citation information: DOI 10.1109/JESTPE.2021.3099476, IEEE Journal of Emerging and Selected Topics in Power Electronics

As shown in Fig. 10, at t_0, v_{C1} is equal to V_1, and i_{s1} is equal to 0. During t_0 to t_1, i_1 is equal to $i_{s1}/2$, hence based on the expression of i_{s1} in (14), the input current can be expressed by

$$i_1(t) = \frac{C_r \omega_r V_1}{2} \sin \omega_r (t - t_0) \tag{40}$$

At t_1, v_{C1} is equal to 0. If ignoring the influence of the dead-band, according to (14) and (40), the maximum average value of input current can be expressed as

$$\overline{i}_{1\_\max} = \frac{2}{T_s} \int_{t_0}^{t_1} i_1(t) dt = 2 f_s C_r V_1 \tag{41}$$

Hence, the maximum transmission power can be calculated by

$$P_{\max} = V_1 \overline{i}_{1\_\max} = 2 C_r f_s V_1^2 \tag{42}$$

From the analysis above, it can be deduced that the maximum power is related to the value of C_r. Hence, the resonant capacitor can be designed according to the maximum power.

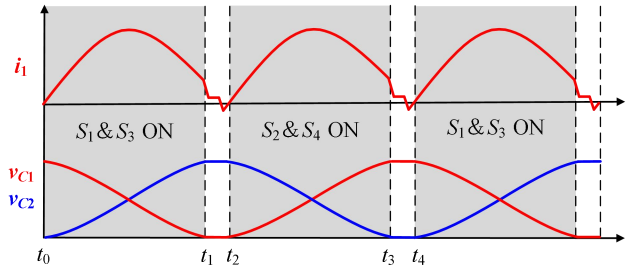

Fig. 10. The waveforms of the input current and the voltages across resonant capacitors at the critical moment when power limitation occurs.

D. Integration of Magnetic Components

As Fig. 2 shows, there are four inductors and one transformer in the proposed converter. The method of magnetic components integration is applied in this paper to reduce the number of magnetic components, and the detailed process is shown in Fig. 11.

Fig. 11(a) shows the magnetic components network of the proposed converter, and its equivalent circuit when L_{r2} and L_{a2} are referred to the primary side is shown in Fig. 11(b). According to the equivalent replacement principle of delta-star connection, the circuit in Fig. 11(b) can be transformed into the T type circuit shown in Fig. 11(c). Then, the cantilever model of the transformer can be obtained from the T type circuit, which is shown in Fig. 11(d). In order to limit the maximum power in a safe range, the value of resonant capacitors cannot be too large. Hence, large resonant inductors are used in the proposed converter to meet the requirement of resonant frequency. Considering that the transformer leakage inductance is small, an external inductor is used to compensate the inadequate value of the transformer leakage inductance. Hence, L_{ca} is divided into two parts, the external series inductor L_{k_ext} and the transformer internal leakage inductance L_{leak}. Hence, as Fig. 11(e) shows, the cantilever model of the actual transformer is the circuit in the red dotted box. Finally, convert the actual transformer from cantilever model to T model, which is shown in Fig. 11(f).

The external inductor in Fig. 11(f) can be calculated by (43).

$$L_{k\_est} = \frac{2 L_r L_a}{2 L_r + L_a} - L_{leak} \tag{43}$$

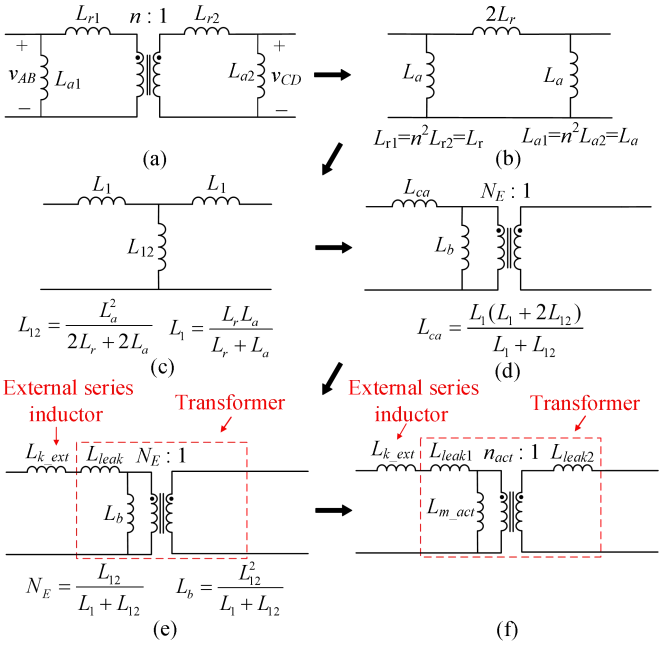

Fig. 11. The integration of the magnetic components.

After the equivalent transformation, the turns ratio of the actual transformer n_{act} in Fig. 11(f) is not equal to the turns ratio n in Fig. 2, and it can be calculated by (44). The magnetizing inductance of the actual transformer in Fig. 11(f) can be calculated by (45).

$$n_{act} = \sqrt{\frac{4L_rL_a + 4L_r^2 + L_a^2}{(2L_r + L_a)^2} - \frac{2L_{k\_ext}(L_a + L_r)}{L_a(2L_r + L_a)}} \tag{44}$$

$$L_{m\_act} = \frac{n_{act} L_a^2}{2(L_a + L_r)} \tag{45}$$

The magnetic core of the transformer can be designed according to (44) and (45). By this method, the auxiliary inductors, resonant inductors and transformer of the C4LC-DCX converter can be simplified and manufactured with one external inductor and one conventional transformer without changing the midpoint voltages and switch currents, which is the meaning of magnetic component integration in this paper.

The final circuit derived by magnetic components integration is shown in Fig. 12, which has the same electrical characteristics of resonant tank as the circuit shown in Fig. 2. The reason why discrete magnetic components are used in the topology shown in Fig. 2 instead of the integrated case is that the topology is completely symmetrical, which can simplify the analysis of operation principle and ZVS condition under bidirectional power flow.

In practical application, the transformer is none-ideal, which includes leakage inductance and magnetizing inductance. The leakage inductance can be used as part of resonant inductor, and the large magnetizing inductance in real transformer has negligible influence on the magnetic components network of the proposed converter. Therefore, in the process of magnetic components integration, the magnetizing inductance is ignored for the circuit shown in Fig. 11(a). It should be noted that the proposed C4LC-DCX converter is implemented by the final circuit derived by magnetic components integration shown in Fig. 12 in the hardware design. In the final circuit, both the leakage inductance and magnetizing inductance of the actual

This article has been accepted for publication in a future issue of this journal, but has not been fully edited. Content may change prior to final publication. Citation information: DOI 10.1109/JESTPE.2021.3099476, IEEE Journal of Emerging and Selected Topics in Power Electronics

transformer are considered.

The magnetic components network of the CLLLC and C4LC converters can be equivalently transformed, but the symmetrical magnetic components network of the proposed converter shown in Fig. 2 simplifies the analysis of operation principle and ZVS condition in bidirectional power directions.

For the resonant tank of conventional CLLLC structure, the parameters in the primary and secondary sides are symmetrical. If clamping diodes are added to achieve power limitation in a safe range, the value of the two resonant inductors will be too large to be implemented by the transformer leakage inductances. Hence, the magnetic components network of the CLLLC converter will be implemented by two external series inductors and one conventional transformer. Besides, when the CLLLC converter operates in resonant point, the voltage conversion gain is equal to the turns ratio. While for the circuit derived by magnetic components shown in Fig. 12, the inductor in the secondary side is the small intrinsic leakage inductance of transformer, hence only one external inductor and one conventional transformer is required, and the turns ratio can be calculated according to (44).

In many engineering practices, when the transformer is used in combination with external series inductor, the leakage inductors of transformer are considered to be small and are ignored. While for the transformer model applied in the circuit derived by magnetic components integration, the actual leakage inductors in the primary and secondary side are taken into account, and the addition of external series inductor is to compensate the inadequate value of the leakage inductors.

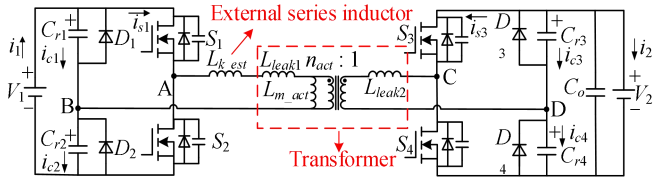

Fig. 12. The final circuit derived by magnetic components integration.

IV. Parameter Design and Experimental Results

A. Parameter Design

A 1000W experimental prototype based on GaN devices which is shown in Fig. 13 is built to verify the above analysis for the proposed converter. The input voltage V_1 and output voltage V_2 are both 400V, and the switching frequency f_s is 500kHz.

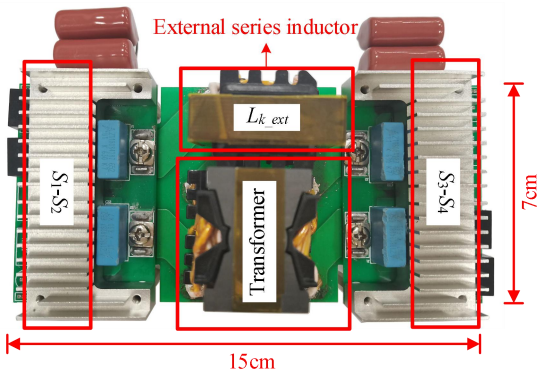

Fig. 13. The experimental prototype.

To reduce the size of converter, the prototype is designed according to the circuit derived by magnetic components integration shown in Fig. 12, in which the four inductors and one transformer of the C4LC-DCX converter shown in Fig. 2 is implemented by one external series inductor and one conventional transformer.

For the C4LC-DCX converter shown in Fig.2, under the condition of V_1=V_2=400V, the turns ratio n can be calculated based on (30).

$$n = \frac{V_1}{V_2} = \frac{400}{400} = 1 \tag{46}$$

The value of the resonant capacitors is related to the maximum transmission power. Under the condition of P_{max}=1.23kW and f_s=500kHz, the value of resonant capacitor can be obtained according to (42).

$$C_r = \frac{P_{\max}}{2 f_s V_1^2} = \frac{1230}{2\times 5\times 10^5 \times 400^2} = 7.7nF \tag{47}$$

Under the condition of t_{dead}=50ns, f_s=f_r=500kHz, C_{oss1}=C_{oss2}=60pF and P_o=1kW, the constraint conditions of the auxiliary inductor can be deduced based on (35), (37) and (39).

$$L_a \le \frac{f_s V_1^2 (1-4 t_{dead} f_r)}{16\pi^2 t_{dead} P_o f_r^3} = 73\mu H \tag{48}$$

$$L_a \le \frac{V_1^2 t_{dead} f_s (1-2 f_r t_{dead})}{16 C_{oss1} f_s f_r V_1^2 + 8\pi^2 t_{dead}^2 f_r^3 P_o} = 60\mu H \tag{49}$$

$$L_a \le \frac{n^2 t_{dead}}{16 f_r C_{oss2}} = \frac{1^2\times 50\times 10^{-9}}{16\times 5\times 10^5 \times 60\times 10^{-12}} = 104\mu H \tag{50}$$

Hence, the auxiliary inductor L_a is designed to be equal to 60μH to ensure that all the switches can achieve full-load range ZVS.

Then, by substituting L_a=60μH, C_r=7.7nF and f_r=500kHz into (9), the value of resonant inductor can be calculated.

$$L_r = \frac{L_a}{8\pi^2 f_r^2 L_a C_r - 1} = 7.3\mu H \tag{51}$$

The leakage inductance of the actual transformer L_{leak} is 2μH. For the final circuit derived by magnetic components integration, the value of the external series inductor can be calculated by substituting L_r=7.3μH and L_a=60μH into (43).

$$L_{k\_est} = \frac{2L_r L_a}{2L_r + L_a} - L_{leak} = 9.7\mu H \tag{52}$$

By substituting the value of L_r, L_a and L_{k_est} into (44), the turns ratio of the actual transformer n_{act} can be calculated.

$$n_{act} = \sqrt{\frac{4L_r L_a + 4L_r^2 + L_a^2}{(2L_r + L_a)^2} - \frac{2L_{k\_ext}(L_a + L_r)}{L_a(2L_r + L_a)}} = 0.84 \tag{53}$$

According to (45), the magnetizing inductance of the actual transformer L_{m_act} can be calculated.

$$L_{m\_act} = \frac{n_{act} L_a^2}{2(L_a + L_r)} = \frac{0.84\times(60\times 10^{-6})^2}{2\times(60\times 10^{-6} + 7.3\times 10^{-6})} = 22.5\mu H \tag{54}$$

TABLE I shows the parameters of the prototype. The parameters selected according to the above method can make the converter resonate at the 500kHz switching frequency.

This article has been accepted for publication in a future issue of this journal, but has not been fully edited. Content may change prior to final publication. Citation information: DOI 10.1109/JESTPE.2021.3099476, IEEE Journal of Emerging and Selected Topics in Power Electronics

TABLE I
PARAMETERS OF THE EXPERIMENTAL PROTOTYPE

Item	Detail
Input Voltage (V_1)	400V
Output Voltage (V_2)	400V
Rated Output Power (P_o)	1000W
Switching Frequency (f_s)	500kHz
Turns Ratio (n)	1
Resonant Capacitance (C_r)	7.7nF
Resonant Inductance (L_r)	7.3μH
Auxiliary Inductance (L_a)	60μH
External Series Inductor (L_{k_set})	9.7μH
Leakage Inductance of Actual Transformer (L_{leak})	2μH
Turns Ratio of Actual Transformer (n_{act})	14:17
Magnetizing Inductor of Actual Transformer (L_{m_act})	22.5μH
Switches	GS66508T
Clamping Diodes	G3S06503C

B. Experimental Results

The steady-state waveforms of the converter under different loads are shown in Fig. 14. v_{gs2} and v_{gs4} are the driving signals of S_2 and S_4 respectively, and i_{rp} is the resonant current in the primary side (i_{rp}=i_{r1}-i_{La1}). It can be seen from Fig. 14(a) and Fig. 14(b) that the driving signals for the primary and secondary bridges are identical under different power directions, and the actual resonant frequency is equal to 500kHz, which verifies the correctness of (7). Fig. 14(c) is the waveforms of the converter in forward power limitation mode, it can be seen that the resonant capacitors are clamped by the conducted diodes in the power limitation mode (1100W), which interrupts the power transmission.

Fig. 15 shows the waveforms of the midpoint voltages (v_{AB} and v_{CD}, where Point A, B, C and D are denoted in Fig. 2) and the resonant currents on both sides of the transformer under different loads in the forward and backward power transmission modes. As Fig. 15 shows, i_{rs} is the resonant current in the secondary side (i_{rs}=i_{r2}-i_{La2}), the voltages across the two auxiliary inductors are nonlinear, and the converter operates effectively under different loads and different power directions.

Fig. 16 shows the soft-switching waveforms of the proposed C4LC-DCX converter under different load conditions. As it is shown in Fig. 16, all the switches in the proposed converter can achieve ZVS at no-load, half-load and full-load conditions under bidirectional power flow.

Fig. 17 shows the dynamic waveforms of the proposed converter. In Fig. 17(a), the power is changed from +500W to -500W. It can be seen that the direction of power flow can be changed smoothly. In Fig. 17(b), the power of the proposed converter switches between 100W and 500W. It can be seen that the output voltage remains unchanged when the load changes in the power transmission mode. The soft-start waveforms of the proposed converter are shown in Fig. 17(c). It can be seen that the inrush current is limited when the converter starts up.

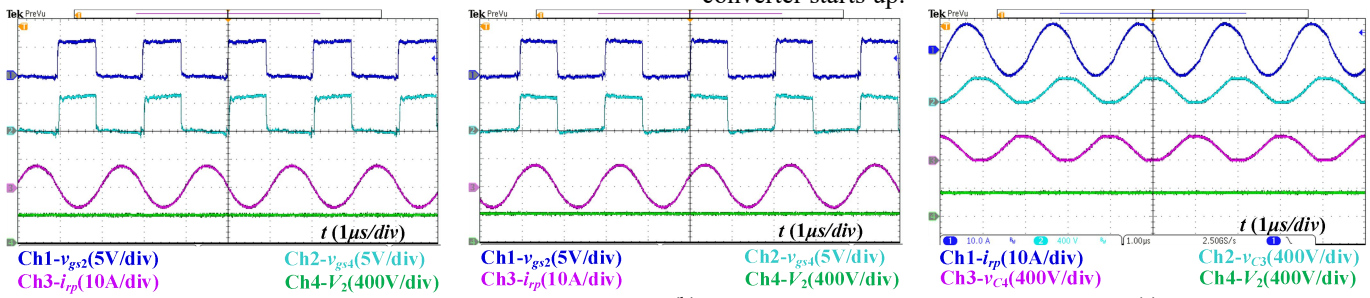

Fig. 14. Steady-state waveforms of the proposed converter under different loads.
(a) Full-load of forward power transmission. (b) Full-load of backward power transmission. (c) Over-load of forward power limitation mode.

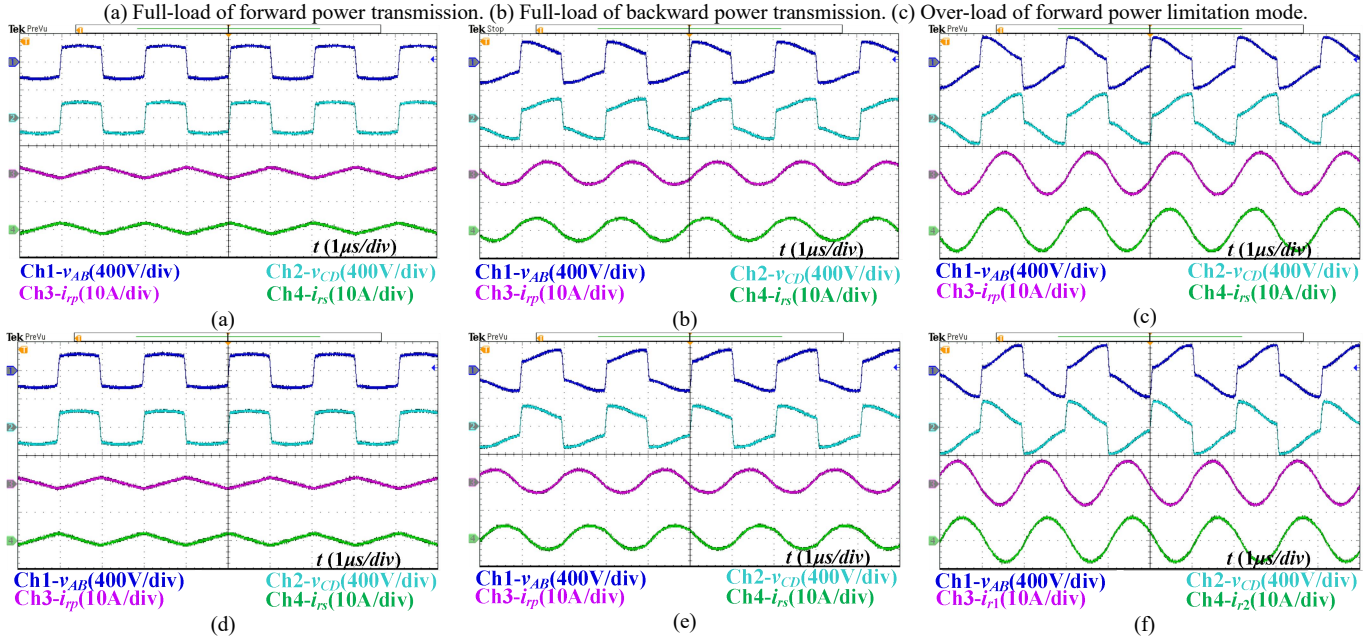

Fig. 15. The waveforms of the midpoint voltages and resonant currents. Forward power transmission: (a) no-load; (b) half-load; (c) full-load. Backward power transmission:(d) no-load; (e) half-load; (f) full-load.

This article has been accepted for publication in a future issue of this journal, but has not been fully edited. Content may change prior to final publication. Citation information: DOI 10.1109/JESTPE.2021.3099476, IEEE Journal of Emerging and Selected Topics in Power Electronics

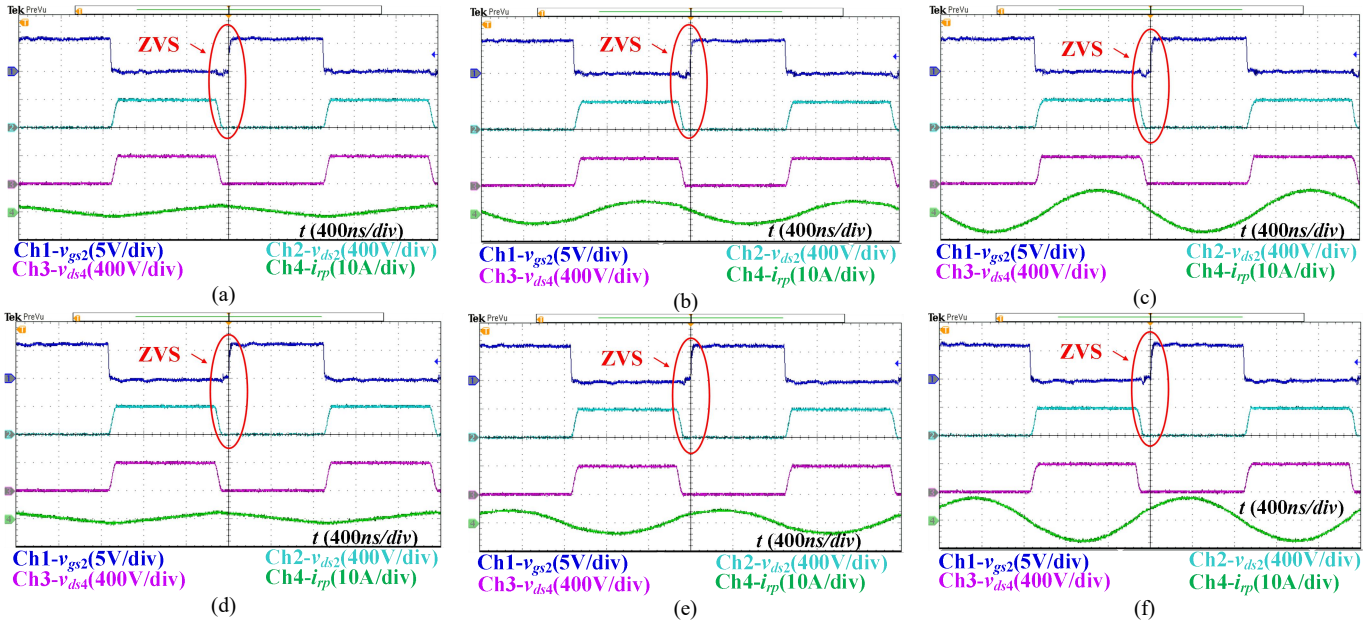

Fig. 16. The soft-switching waveforms of the C4LC-DCX converter. Forward power transmission: (a) no-load; (b) half-load; (c) full-load. Backward power transmission: (d) no-load; (e) half-load; (f) full-load.

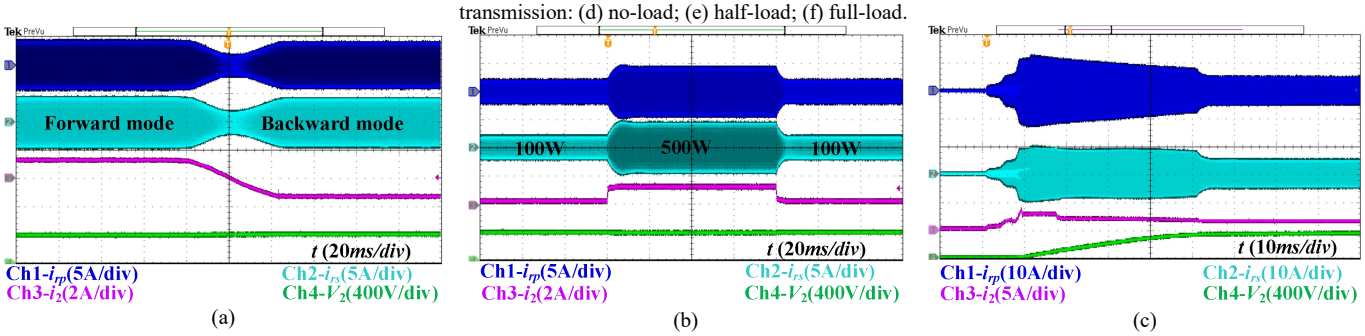

Fig. 17. The dynamic waveforms of the proposed converter.
(a) Forward mode to backward mode. (b) Load changes between 100W and 500W. (c) The soft-start waveforms.

Fig. 18 shows the measured voltage gain and efficiency of the proposed C4LC-DCX resonant converter.

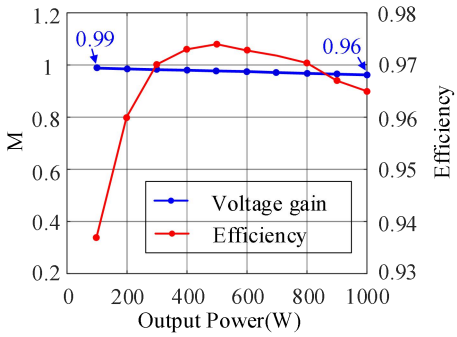

Fig. 18. The measured voltage gain and efficiency.

It can be seen from Fig. 18 that the voltage gain of the proposed converter is almost constant under different load conditions. The gain drops slightly with the increase of the output power, which could be caused by the conduction resistance, the line impedance, etc. The maximum efficiency of the proposed converter is 97.4% and the full-load efficiency is 96.5% at 500kHz.

V. Conclusion

In this paper, a bidirectional symmetrical C4LC-DCX resonant converter with the synchronous PWM modulation method is proposed for DCX application. By adding auxiliary inductors, full load range ZVS considering the effect of load and switch junction capacitors for all the switches can be achieved. With the method of magnetic components integration, the number of magnetic components is reduced. In addition, over current protection and power limitation capability are embedded in the proposed converter by adding clamping diodes. A 1-kW prototype is designed to verify the theoretical analysis. The ZVS analysis and parameter design are verified by the experimental results. Meanwhile, the results have shown that natural bidirectional power flow, constant voltage conversion gain and natural power limitation capability can be obtained with the proposed solution.

References

[1] J. Teng, S. Chen, S. Luan and J. Xu, "Bidirectional DC-DC Converter with a Wide-Range Voltage Conversion Ratio," in *Proc. 4th Int. Future Energy Electron. Conf.*, Singapore, 2019, pp. 1-6.

[2] P. He and A. Khaligh, "Comprehensive Analyses and Comparison of 1 kW Isolated DC-DC Converters for Bidirectional EV Charging Systems," *IEEE Trans. Transp. Electrific.*, vol. 3, no. 1, pp. 147-156, Mar. 2017.

[3] G. Xu, L. Li, X. Chen, Y. Liu, Y. Sun and M. Su, "Optimized EPS Control to Achieve Full Load Range ZVS with Seamless Transition for Dual Active Bridge Converters," *IEEE Trans. Ind. Electron.*, Early Access. DOI: 10.1109/TIE.2020.3014562.

[4] H. Akagi, S. Kinouchi and Y. Miyazaki, "Bidirectional isolated dual-active-bridge (DAB) DC-DC converters using 1.2-kV 400-A SiC-MOSFET dual modules," *CPSS Trans. Power Electron. Appl.*, vol. 1, no. 1, pp. 33-40, Dec. 2016.

[5] S. A. Gorji, M. Ektesabi and J. Zheng, "Isolated switched-boost push-pull DC-DC converter for step-up applications," *IET Electron. Lett.*, vol. 53, no. 3, pp. 177-179, Feb. 2017.

[6] H. Wang and Z. Li, "A PWM LLC Type Resonant Converter Adapted to Wide Output Range in PEV Charging Applications," *IEEE Trans. Power Electron.*, vol. 33, no. 5, pp. 3791-3801, May 2018.

[7] C. Zhang, P. Li, Z. Kan, X. Chai and X. Guo, "Integrated Half-Bridge CLLC Bidirectional Converter for Energy Storage Systems," *IEEE Trans. Power Electron.*, vol. 65, no. 5, pp. 3879-3889, May 2018.

[8] X. Liu et al., "Novel dual-phase-shift control with bidirectional inner phase shifts for a dual-active-bridge converter having low surge current and stable power control, " *IEEE Trans. Power Electron.*, vol. 32, no. 5, pp. 4095-4106, May 2017.

[9] X. Wu, H. Chen, and Z. Qian, "1-MHz LLC resonant DC transformer (DCX) with regulating capability," *IEEE Trans. Ind. Electron.*, vol. 63, no. 5, pp. 2904-2912, May 2016.

[10] Y. Liao et al., "Single-stage DAB-LLC Hybrid Bidirectional Converter with Tight Voltage Regulation under DCX Operation," *IEEE Trans. Ind. Electron.*, Early Access. DOI: 10.1109/TIE.2020.3014562.

[11] H. Ma, W. Liu, J. Wang, C. Zheng and G. Lu, "Two-stage power supply based on double resonant tank LLC-DCX for magnetic levitation control system applications," in *Proc. IEEE Appl. Power Electron. Conf. Expo.*, Charlotte, NC, 2015, pp. 3195-3200.

[12] M. Fu, C. Fei, Y. Yang, Q. Li and F. C. Lee, "Optimal Design of Planar Magnetic Components for a Two-Stage GaN-Based DC-DC Converter," *IEEE Trans. Power Electron.*, vol. 34, no. 4, pp. 3329-3338, Apr. 2019.

[13] Öztürk Şahin Alemdar, Ozan Keysan, "Design and Implementation of an Unregulated DC-DC Transformer (DCX) Module using LLC Resonant Converter," in *Proc. 8th IET Int. Conf. Power Electron.*, Glasgow, Scotland, 2016, pp. 1-6.

[14] J. Park and K. Lee, "A two-stage bidirectional DC/DC converter with SiC-MOSFET for vehicle-to-grid (V2G) application," in *Proc. IEEE Conf. Energy Convers.*, Kuala Lumpur, Malaysia, 2017, pp. 288-293.

[15] S. Lu, K. Sun, G. Cao, Z. Yi, H. Liu and Y. Li, "A High Efficiency and High Power SiC DC-DC Converter Based on Interleaved-Boost and Full-bridge LLC Integration for PV Applications," in *Proc. IEEE Energy Convers. Congr. Expo.,* Detroit, MI, USA, 2020, pp. 4822-4827.

[16] X. Sun, J. Qiu, X. Li, B. Wang, L. Wang and X. Li, "An improved wide input voltage buck-boost+LLC cascaded converter," in *Proc. IEEE Energy Convers. Congr. Expo.*, Montreal, QC, Canada, 2015, pp. 1473-1478.

[17] W. Feng, P. Mattavelli and F. C. Lee, "Pulsewidth Locked Loop (PWLL) for Automatic Resonant Frequency Tracking in LLC DC-DC Transformer (LLC-DCX)," *IEEE Trans. Power Electron.*, vol. 28, no. 4, pp. 1862-1869, Apr. 2013.

[18] S. Jiang, W. Zhang, B. Liu and F. Wang, "Automatic resonant frequency tracking in unregulated LLC resonant converters based on total resonant current harmonic calculation," in *Proc. IEEE Energy Convers. Congr. Expo.*, Denver, CO, 2013, pp. 4193-4198.

[19] O. Yu, C. Yeh, M. Lee and J. Lai, "Drain-Source Synchronous Rectification Efficiency and Light-Load Stability Improvement through Multi-Level Turn-Off for LLC-based DC-DC Converters," in *Proc. IEEE Energy Convers. Congr. Expo.*, Baltimore, MD, USA, 2019, pp. 6462-6467.

[20] C. Fei, M. H. Ahmed, F. C. Lee and Q. Li, "Dynamic bus voltage control for light load efficiency improvement of two-stage voltage regulator," in *Proc. IEEE Energy Convers. Congr. Expo.*, Milwaukee, WI, 2016, pp. 1-8.

[21] M. H. Ahmed, F. C. Lee, Q. Li and M. d. Rooij, "Design Optimization of Unregulated LLC Converter with Integrated Magnetics for Two-Stage 48V VRM," in *Proc. IEEE Energy Convers. Congr. Expo.,* Baltimore, MD, USA, 2019, pp. 521-528.

[22] J. Jung, H. Kim, M. Ryu and J. Baek, "Design Methodology of Bidirectional CLLC Resonant Converter for High-Frequency Isolation of DC Distribution Systems," *IEEE Trans. Power Electron.*, vol. 28, no. 4, pp. 1741-1755, Apr. 2013.

[23] Z. Lv, X. Yan, Y. Fang and L. Sun, "Mode analysis and optimum design of bidirectional CLLC resonant converter for high-frequency isolation of DC distribution systems," in *Proc. IEEE Energy Convers. Congr. Expo.*, Montreal, QC, Canada, 2015, pp. 1513-1520.

[24] Minjae Kim, Shinyoung Noh, and Sewan Choi, "New Symmetrical Bidirectional L3C Resonant DC-DC Converter with Wide Voltage Range," in *Proc. IEEE Appl. Power Electron. Conf. Expo.*, 2016, pp.859-863.

[25] X. Yan, B. Zhang, X. Xiao, H. Zhao, and L. Yang, "A bidirectional power converter for electric vehicles in V2G systems," in *Proc. IEEE Int. Electric Mach. Drives Conf*, 2013, pp. 254-259.

[26] Jingtao Xu, Jian Yang, and Guo Xu, "PWM Modulation and Control Strategy for LLC-DCX Converter to Achieve Bidirectional Power Flow in Facing With Resonant Parameters Variation," *IEEE Access*, vol.7, pp.54693-54704, Apr. 2019.

[27] Xiaoying Chen, Guo Xu, and Shiming Xie, "A Natural Bidirectional Input-Series-Output-Parallel LLC-DCX Converter with Automatic Power Sharing and Power Limitation Capability for Li-Ion Battery Formation and Grading System," *IEEE J. Emerg. Sel. Topics Power Electron.*, vol. 8, no. 4, pp. 3618-3632, Dec. 2020.

[28] T. Jiang, J. Zhang, X. Wu, K. Sheng, and Y. Wang, "A bidirectional LLC resonant converter with automatic forward and backward mode transition," *IEEE Trans. Power Electron.,* vol. 30, no. 2, pp. 757-770, Feb. 2015.

[29] C. Chen, X. Zhao, C. Yeh and J. Lai, "Analysis of the Zero-Voltage Switching Condition in LLC Series Resonant Converter with Secondary Parasitic Capacitors," in *Proc. IEEE Appl. Power Electron. Conf. Expo.*, Anaheim, CA, USA, 2019, pp. 828-832.

[30] B. Yang, F. C. Lee and M. Concannon, "Over current protection methods for LLC resonant converter," in *Proc. IEEE Appl. Power Electron. Conf. Expo.*, 2003, pp.605-609.

[31] F. Dianbo, F. C. Lee, L. Ya, and X. Ming, "Novel multi-element resonant converters for front-end dc/dc converters," in *Proc. IEEE Power Electron. Special., Conf.,* 2008, pp. 250-256.

[32] X. Xie, J. Zhang, C. Zhao, Z. Zhao, and Z. Qian, "Analysis and optimization of LLC resonant converter with a novel over-current protection circuit," *IEEE Trans. Power Electron.*, vol. 22, no. 2, pp. 435-443, Mar. 2007.

[33] L. Wang, Q. Zhu, W. Yu and A. Q. Huang, "A Medium-Voltage Medium-Frequency Isolated DC-DC Converter Based on 15-kV SiC MOSFETs," *IEEE J. Emerg. Sel. Topics Power Electron.*, vol. 5, no. 1, pp. 100-109, Mar. 2017.

[34] G. Deng et al., "ZVS Analysis of Half Bridge LLC-DCX Converter Considering the Influence of Resonant Parameters and Loads," in *Proc. IEEE Energy Convers. Congr. Expo.*, Detroit, MI, USA, 2020, pp. 1186-1190, 2020.